


# Single-Crystalline $\text{Cu}_4\text{Bi}_4\text{S}_9$ Nanoribbons: Facile Synthesis, Growth Mechanism, and Surface Photovoltaic Properties

Hongxing Li,<sup>†,‡</sup> Qinglin Zhang,<sup>†</sup> Anlian Pan,<sup>\*,†</sup> Yanguo Wang,<sup>\*,†,§</sup> Bingsuo Zou,<sup>†</sup> and Hong Jin Fan<sup>\*,‡</sup>

<sup>†</sup>College of Physics and Microelectronics Science, Key Laboratory for Micro-Nano Physics and Technology of Hunan Province, Hunan University, Changsha 410082, People's Republic of China

<sup>‡</sup>Division of Physics and Applied Physics, School of Physical and Mathematical Sciences, Nanyang Technological University, 21 Nanyang Link, 637371 Singapore

<sup>§</sup>Institute of Physics, Chinese Academy of Sciences, P.O. Box 603, Beijing 100080, People's Republic of China

 Supporting Information

**ABSTRACT:** Cu-based ternary chalcogenides have received great interest as low-cost alternatives to conventional photovoltaic materials. In this work, a large quantity of single-crystalline, orthorhombic phase  $\text{Cu}_4\text{Bi}_4\text{S}_9$  nanoribbons are fabricated using a facile solvothermal method. The growth of the  $\text{Cu}_4\text{Bi}_4\text{S}_9$  nanoribbons is revealed to be a layer-by-layer stacking of  $\text{Cu}_4\text{Bi}_4\text{S}_9$  thin slabs via dodecylamine (DDA) linker, in which the number of stacking layers, and, subsequently, the width-to-thickness ratio, depends on the DDA concentration. Optical investigations show that the as-prepared  $\text{Cu}_4\text{Bi}_4\text{S}_9$  nanoribbons have a narrow bandgap of  $E_g = 1.14$  eV and enhanced surface photovoltage response in the entire visible wavelength range. It is indicated that these  $\text{Cu}_4\text{Bi}_4\text{S}_9$  nanoribbons have potential application in photodetectors, solar cells, or other optoelectronic devices.

**KEYWORDS:** chalcogenide,  $\text{Cu}_4\text{Bi}_4\text{S}_9$ , nanobelts, solvothermal, surface photovoltage, photovoltaics

## INTRODUCTION

One-dimensional (1D) structures such as nanowires and nanoribbons have been receiving increased interest, because of their application potential in energy-harvesting devices such as photovoltaics (PVs) and batteries.<sup>1–3</sup> Nanowire-based solar cells are regarded as a promising class of PV devices, because of several performance and processing benefits that are enabled by their 1D geometry.<sup>4,5</sup> The large aspect ratio of nanowires maximizes the light absorption, and their nanoscale width permits much free movement and more-efficient collection of electrons.<sup>1</sup> The availability of 1D nanostructures with well-defined morphologies and dimensions should enable new types of applications or enhance the performance of currently existing photoelectric devices.

Various physical and chemical methods have been developed for the synthesis of 1D nanostructures of controllable size and shape, including vapor–liquid–solid (VLS)<sup>6–8</sup> and solution–liquid–solid (SLS) processes,<sup>9</sup> solvothermal,<sup>10,11</sup> template-assisted,<sup>12</sup> and thermolysis of a single-source precursor in a ligating solvent.<sup>13</sup> Compared with the numerous publications on elemental and binary 1D materials, there are less reports on the controlled synthesis of ternary semiconductors with 1D morphology.

Copper-based multicomponent chalcogenides (CBMC) is a system of technological importance for PV energy conversions. For example, the most-studied  $\text{CuIn}_x\text{Ga}_{1-x}\text{Se}_2$  system holds the efficiency record ( $\sim 20\%$ ) for thin-film polycrystalline solar cells.<sup>14</sup> In addition, the earth-abundant materials  $\text{Cu}_2\text{ZnSnS}_4$  fulfill the requirement for the green and low-cost manufacture of PV devices.<sup>15,16</sup> As a key member of the CBMC family, the Cu–Bi–S compounds consist of the earth-abundant and inexpensive elements of Bi and S, and therefore has attracted recent efforts in

fabrication and investigation of their properties. Haber et al.<sup>17</sup> reported that the narrow band gap (1.3 eV) and high absorption coefficient (up to  $10^5$   $\text{cm}^{-1}$ ), as well as the good electrical conductivity (84  $\Omega$  cm) of polycrystalline  $\text{Cu}_3\text{BiS}_3$  film, make itself highly useful as a light absorber layer in solar cells. In 2003, Nair et al.<sup>18</sup> demonstrated the outstanding photoresponse characteristics of  $\text{Cu}_3\text{BiS}_3$  thin films. Several approaches have been developed to fabricate Cu–Bi–S compound films, including vacuum annealing,<sup>19</sup> physical vapor deposition, and sputter coating.<sup>20</sup> However, to the best of our knowledge, 1D Cu–Bi–S nanostructures, specifically the Cu–Bi–S nanoribbons, have rarely been reported,<sup>21,22</sup> because of the great challenge in composition and phase control during the synthesis processes.

The solvothermal method is a powerful tool for the controllable synthesis of 1D semiconductor nanostructures at low temperatures.<sup>23</sup> Organic–ligand molecules (e.g., alkylamines, fatty acids, alkyl thiols) are often used as solvents and/or capping agents to prepare nanoscale inorganic semiconductors. These organic–ligand molecules contain both metal coordinating groups and solvophilic groups, which can attach selectively to crystallographic faces and dynamically control the nanoscopic morphologies of the final products. In recent years, remarkable progress has been achieved in the shape control of 1D nanomaterials by means of solvothermal reaction. For example, Gao et al. reported the large-scale fabrication of ultrathin lamellar mesostructured  $\text{CoSe}_2$ -DETA (DETA diethylenetriamine) hybrid nanobelts in a

**Received:** November 22, 2010

**Revised:** January 6, 2011

**Published:** January 20, 2011

binary solution of organic amine and water under mild solvothermal conditions.<sup>24</sup> Single-crystalline Ag<sub>2</sub>S nanowires were also prepared by Li and co-workers<sup>25</sup> through the solvothermal process that uses dodecylamine as the capping reagent.

The surface photovoltage (SPV) method is a well-established, contactless, and nondestructive technique for the characterization of semiconductors, which relies on analyzing the illumination-induced changes in the surface voltage.<sup>26,27</sup> The signal of photovoltage is attributed to the changes of surface potential barriers before and after light illumination. It can offer detailed, quantitative information on intrinsic properties of semiconductors (e.g., bandgap, surface states, photogenerated charges separation). SPV technology has been successfully employed for the study of the charge transfer in photostimulated surface interaction, dye sensitization process, and photocatalysis.<sup>26,27</sup>

In this article, we report our successful large-yield synthesis of single-crystalline Cu<sub>4</sub>Bi<sub>4</sub>S<sub>9</sub> (CBS) nanoribbons via a facile solvothermal process. Data from systematic control experiments will be shown, which suggest that the nanoribbons form via stacking of individual CBS thin slabs via the dodecylamine (DDA) linker. The concentration of the linker influences the stacking level, thus allowing a control in the width-to-thickness ratio of the resulting nanoribbons. To explore their potential optoelectronic applications, the as-obtained CBS nanoribbons are characterized using SPV, which reveals an enhanced photovoltage response to the entire visible range of the solar spectrum.

## EXPERIMENTAL SECTION

**Material Synthesis.** In a typical synthesis of CBS nanoribbons, 0.5 mmol of CuCl, 0.5 mmol of BiCl<sub>3</sub>, and 0.70 g of dodecylamine (DDA) were added into a 50-mL three-neck flask containing 30 mL of toluene. The flask was then heated to 70 °C and maintained at this temperature for 30 min under a constant stirring until a blue transparent solution was observed. Then, 250 μL of CS<sub>2</sub> was injected into the solution slowly, and the blue solution turned into a nut-brown colloid. Next, the colloid was transferred into a Teflon-lined stainless-steel autoclave. The autoclave was sealed and maintained at 200 °C for 30 h and then cooled naturally to room temperature. The CBS nanoribbons were collected and washed thoroughly using absolute ethanol and dried under vacuum at 60 °C for 4 h.

**Characterization.** The powder X-ray diffraction (XRD) patterns were recorded with a Bruker Model D8 Advance X-ray powder diffractometer with Cu Kα radiation. The size and morphology of as-synthesized samples were determined using a Hitachi Model S-4800 field-emission scanning electron microscopy (SEM) system, and JEOL Model 3010F high-resolution transmission electron microscopy (TEM) system. Analysis using a SEM system equipped for energy-dispersive X-ray (EDX) spectroscopy was performed to determine the composition of the products. X-ray photoemission spectroscopy (XPS) measurements were performed on a PHI5000c XPS system, using C 1s as a reference. The diffuse reflectance spectrum was characterized using a UV/vis/NIR spectrophotometer (PE Lambda 750 UV) that was equipped with a 60-mm integrating sphere.

**Surface Photovoltage (SPV) Measurements.** The sample was sandwiched between two blank ITO electrodes. Chopped light (~20 Hz) from a 50-W halogen-tungsten lamp connected to a grating monochromator was used as the excitation light source and focused on the sample surface. The SPV signal was capacitively coupled out and measured by a lock-in amplifier (Model SR830). The surface photovoltage (SPV) intensity was not normalized according to the photon energy of halogen-tungsten lamp. The correlated phase spectra were taken synchronously with the SPV spectra.

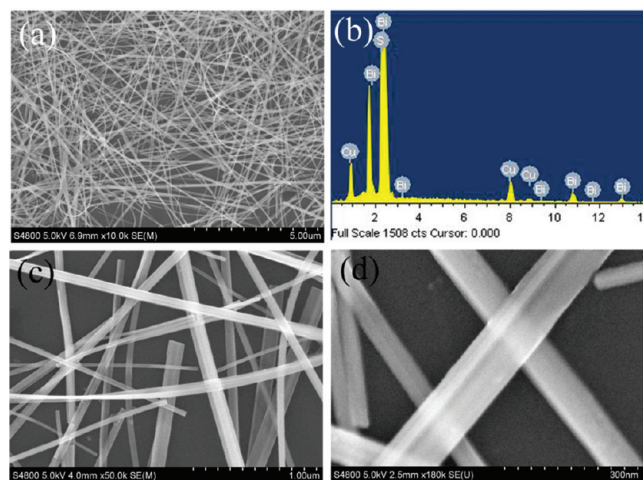


**Figure 1.** (a) Low-magnification SEM image of the CBS nanoribbons dispersed on a Si substrate. (b) EDX pattern of the CBS nanoribbons. (c, d) High-magnification SEM images of the nanoribbons.

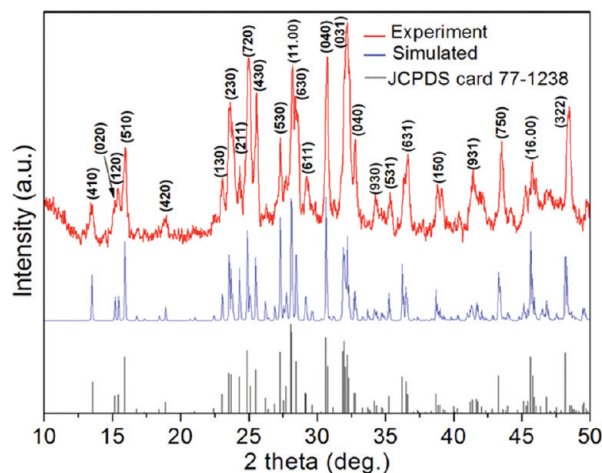


**Figure 2.** Powder XRD pattern of the CBS nanoribbons.

## RESULTS AND DISCUSSION

The morphology of the products was first observed via SEM. Figure 1a shows a typical low-magnification SEM image of the as-grown CBS nanoribbons, which illustrates the large yield of our synthesis (additional SEM images are shown in Figure S1 in the Supporting Information). The CBS nanoribbons have a length up to several hundreds of micrometers and widths of 30–100 nm, resulting in aspect ratios (length to width) up to 10 000. Their ribbonlike structure can be seen more clearly from the high-magnification SEM images (see Figures 1c and 1d). According to the EDX analysis (see Figure 1b), the nanoribbons are composed of Cu, Bi, and S, without any other impurity elements detected. The crystal phase of the as-synthesized product was identified by XRD (Figure 2). All the diffraction peaks can be indexed based on the orthorhombic-phase Cu<sub>4</sub>Bi<sub>4</sub>S<sub>9</sub> (JCPDS File Card No. 77-1238; *a* = 31.528 Å, *b* = 11.622 Å, *c* = 3.951 Å; space group *Pbnm*).

The TEM image (see Figure 3a) further confirms the uniform and smooth surface of the CBS nanoribbons along their total lengths. The high single-crystalline quality of the nanoribbons is revealed by the high-resolution TEM images (see, e.g., Figure 3b). The measured lattice spacing of ~1.16 nm is consistent with the

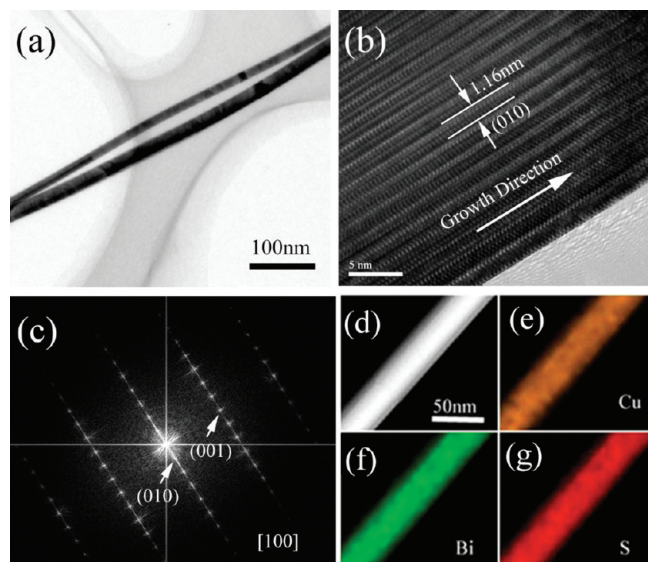


**Figure 3.** (a) TEM image and (b) HRTEM image of the CBS nanoribbons. (c) Corresponding fast Fourier transform (FFT) pattern of the image in panel b. (d) STEM image of the CBS nanoribbons, along with the corresponding 2D-projected STEM elemental mapping for (e) Cu, (f) Bi, and (g) S.

*d*-spacing of (010) planes in orthorhombic  $\text{Cu}_4\text{Bi}_4\text{S}_9$ . Also, the corresponding fast Fourier transform (FFT) image (Figure 3c) can also be well-indexed to the (001) and (010) planes along the [100] zone axis of orthorhombic  $\text{Cu}_4\text{Bi}_4\text{S}_9$ . Therefore, the preferential growth direction of the CBS nanoribbons is along the [001] direction (i.e., the *c*-axis).

Scanning TEM (STEM) EDX was utilized to further verify the elemental composition, as well as the nanoscale spatial uniformity of element distribution, across the nanoribbons. Figure 3d is the STEM image of an examined nanoribbon, and Figures 3e–g are the corresponding 2D-projected STEM elemental mapping for elements Cu, Bi, and S, respectively. All the elements are homogeneously distributed along the length and width of the nanoribbon. The oxidation states of copper, bismuth, and sulfur in the nanoribbons are identified by XPS. The XPS survey spectra (Figure 4) show that the as-obtained sample consists of the elements Cu, Bi, and S, with no obvious impurities. The  $\text{Cu } 2p_{3/2}$  peak at 932.5 eV (Figure 4b) and the  $\text{Bi } 4f_{7/2}$  peak at 158.0 eV (Figure 4c) are consistent with the reported binding energies for  $\text{Cu}^+$  and  $\text{Bi}^{3+}$ ; the peak of  $\text{S } 2p_{3/2}$  at 161.2 eV overlapped with  $\text{Bi } 4f$ , which creates difficulty for the detailed identification.<sup>28</sup> No  $\text{Cu } 2p_{3/2}$  satellite peak at  $\sim 942$  eV that could be attributed to  $\text{Cu}^{2+}$  was detected.<sup>29</sup> Altogether, the above data verify that these ternary alloy CBS nanoribbons obtained through our solvothermal method are of high crystalline quality.

Data of control experiments reveal that addition of an organoamine (dodecylamine is used in this work) has a significant role in determining the final morphology of the product. The surfactant DDA mediates the crystal structure growth and even controls the width-to-thickness ratio. The aforementioned nanoribbons were obtained by adding 0.7 g DDA into the mixed solution (see the Experimental Section). However, when the dosage of DDA was varied, even slightly, the morphology of the products changed dramatically. When the dosage of DDA was changed to 0.6 g while the other conditions such as temperature, reaction time, and volume of toluene remained the same, we

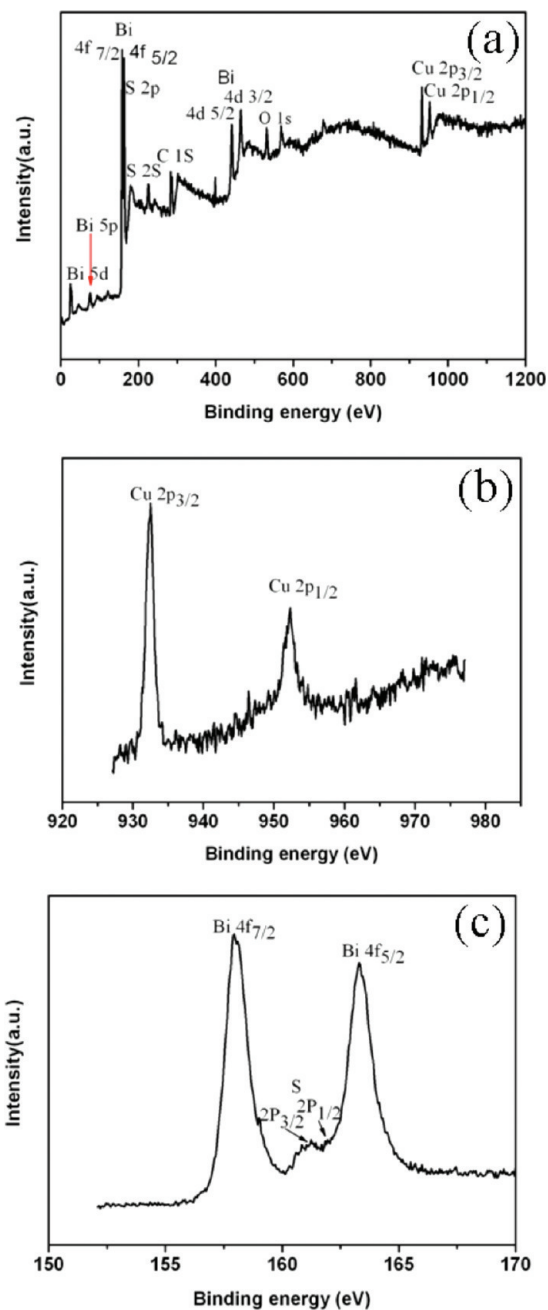


**Figure 4.** (a) XPS spectrum of as-prepared single-crystalline  $\text{Cu}_4\text{Bi}_4\text{S}_9$  nanoribbons in the energy range of 0–1200 eV. (b) High-resolution XPS for  $\text{Cu}^+$ , and (c) high-resolution XPS spectrum of the  $\text{Bi}_{4f}$  overlapped with the  $\text{S}_{2p}$ .

could obtain wide nanobelts (see Figure 5a and 5c), with a width-to-thickness ratio that was much larger than the nanoribbons. The composition of the nanobelts was ascertained by XRD to also be orthorhombic  $\text{Cu}_4\text{Bi}_4\text{S}_9$  (data not shown here). However, when the dosage was increased to 0.75 g, the morphology of the product is wirelike with a reduced width-to-thickness ratio (see Figures 5b and 5d). Figure S2 in the Supporting Information shows the SEM images of the morphology variation from a series of control experiments with different dosage of DDA, from which one can clearly see the dominating effect of the DDA concentration in the mixed solution on the width-to-thickness aspect of the nanoribbons.

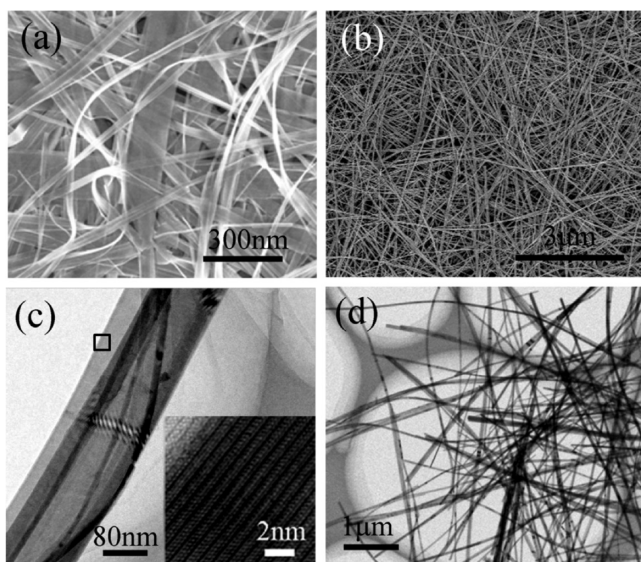


**Figure 5.** (a) SEM image of the CBS nanobelts with larger width-to-thickness ratio prepared with a lower concentration of DDA. (b) SEM image of the ultralong CBS nanowires obtained at a higher concentration of DDA. (The amount of DDA added into the mix solution is 0.60 g in panel a and 0.75 g in panel b, respectively.) (c,d) Corresponding TEM images of the nanobelts and nanowires in panels a and b. Inset is the HRTEM image of the nanobelt.

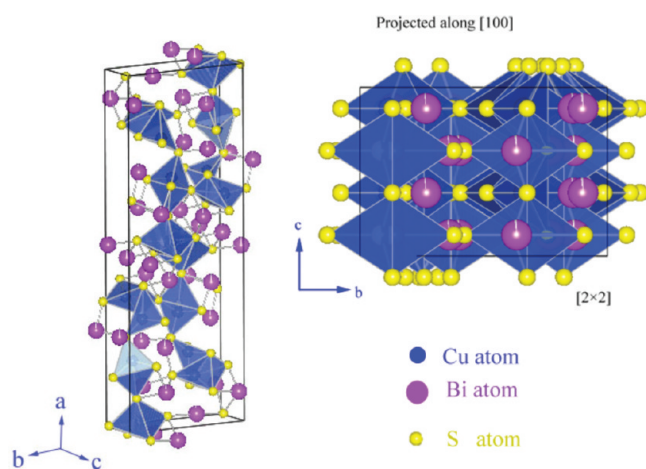
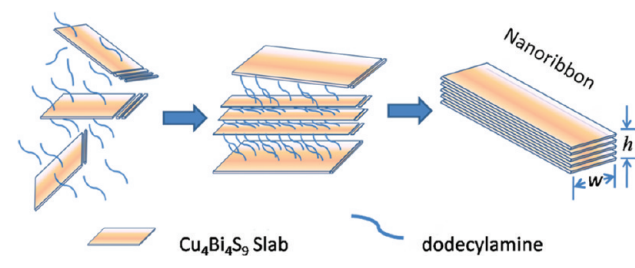


**Figure 6.** Schematic showing the unit-cell structure of  $\text{Cu}_4\text{Bi}_4\text{S}_9$  (right) and the atomic arrangement in the  $\text{Cu}_4\text{Bi}_4\text{S}_9$  supercell  $[2 \times 2]$  structure projected along the  $[100]$  axis (left).

It is well-known that the solvothermal method is successful in the synthesis of nanowires,<sup>25</sup> nanoribbons,<sup>30</sup> and nanotubes.<sup>31</sup> In contrast to other synthetic strategies, such as VLS or template methods, the solvothermal method generally needs no metal catalyst to serve as the energetically favorable site for direct absorption of gas-phase reactant molecules, nor is a spatial-confinement template required to guide the directional growth of nanowires. Thus, it is reasonable to imagine that the driving force of the anisotropic growth of the 1D  $\text{Cu}_4\text{Bi}_4\text{S}_9$  nanostructure originates from the inherent crystal structure of  $\text{Cu}_4\text{Bi}_4\text{S}_9$  materials and the structure-directing role of the DDA molecules. In the supercell structure of the orthorhombic  $\text{Cu}_4\text{Bi}_4\text{S}_9$  (as shown in Figure 6), the lattice constant along

### Scheme 1. Schematics of the Formation Mechanism of the $\text{Cu}_4\text{Bi}_4\text{S}_9$ Nanoribbons in a DDA/Toluene Mixed Solution



the  $[001]$  direction is much smaller than those of the  $[010]$  and  $[100]$  directions.<sup>32,33</sup> According to the Bravais–Friedel–Donnay–Harker (BFDH) law,<sup>34,35</sup> the preferential growth direction of such a crystal is proportional to  $1/d_{hkl}$ . Since the value of  $1/d_{001}$  is much larger than  $1/d_{010}$  and  $1/d_{100}$ , the growth rate along the  $[001]$  direction is therefore higher than the other two directions, accounting for the longitudinal direction along the  $c$ -axis. The side surfaces of the nanoribbon are expected to be  $\{100\}$  and  $\{010\}$ , which is consistent with the TEM observation (see Figure 3b). HRTEM observations show that all the quasi-1D nanostructures (i.e., the nanobelts, nanoribbons, and nanowires) have the same growth direction.

We now propose the formation mechanism of the  $\text{Cu}_4\text{Bi}_4\text{S}_9$  ribbon, as well as a belt and wire structure. At the first stage, very thin  $\text{Cu}_4\text{Bi}_4\text{S}_9$  slabs form as a result of the characteristic crystal anisotropy, linked by the DDA molecules through the interaction between the ligands of the DDA, and the Cu and Bi of the  $\text{Cu}_4\text{Bi}_4\text{S}_9$  framework. (See Figure S3 in the Supporting Information.<sup>10,36</sup>) These slab nuclei then grow further along the  $c$ -axis and stack together via entanglement of the hydrophobic chains of DDAs, forming the layer-by-layer ribbonlike structure, as shown in Scheme 1. This occurs at an optimal DDA dosage (viz., 0.7 g into the solution). When the DDA concentration in the mixed solution is reduced (e.g., 0.5 g), the structure-directing role of the DDA weakens accordingly. As a result, only a limited number of layers of  $\text{Cu}_4\text{Bi}_4\text{S}_9$  slabs can be linked, corresponding to thin nanobelts (see Figure S2a in the Supporting Information). Figure 7 shows TEM and HRTEM images at the edge of one underdeveloped nanobelt. As seen, a clearly visible set of strips (black/white contrast) are running parallel to the longitudinal direction of the nanobelt. These images give support to the belief that the 1D  $\text{Cu}_4\text{Bi}_4\text{S}_9$  nanostructures are indeed formed via layer-by-layer stacking of thin  $\text{Cu}_4\text{Bi}_4\text{S}_9$  slabs. On the other hand, when the DDA concentration exceeds the critical value of  $\sim 0.7$  g, the  $\text{Cu}_4\text{Bi}_4\text{S}_9$  nanoslabs have a higher tendency to stack together to form thicker pallets, because the widths and thicknesses are comparable. This corresponds to the wirelike structure with more square cross sections. With further increases in the DDA dosage to  $>0.80$  g, the obtained product still has a quasi-1D nanostructure, but now it is in the form of nanowire bundles with overall diameters of 200–400 nm (see Figures S2e and S2f in the Supporting Information). This is possibly because the high density of DDA molecules on the interface of the nanowires interlink with each other, so that the nanowires are brought together into bundles. Hence, in this proposed formation mechanism, the quasi-1D structure of the nanobelts in the DDA/toluene binary solvent is predetermined by the inherent crystal structure of  $\text{Cu}_4\text{Bi}_4\text{S}_9$  and the width-to-thickness ratios are regulated by the interaction

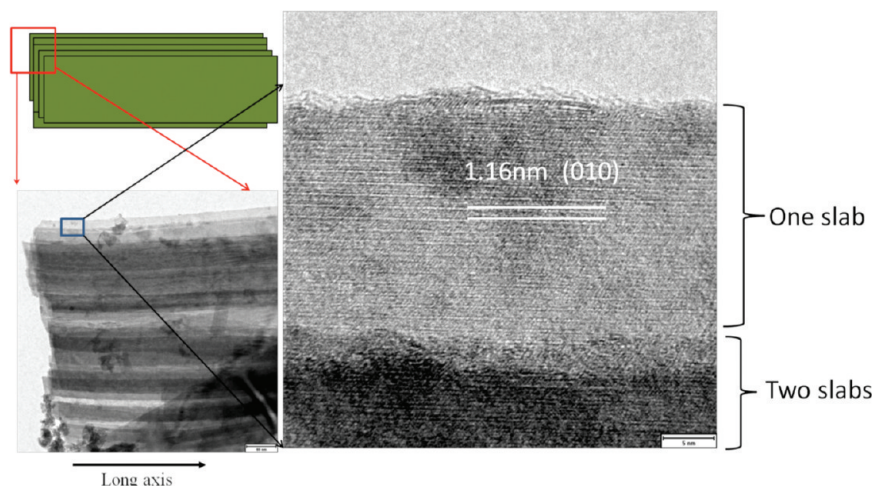


**Figure 7.** TEM and HRTEM images of the nanobelts obtained when 0.5 g of DDA was used in the mixed solution, from which we can see that the wide nanobelt is formed by layer-by-layer stacking of ultrathin nanoribbons parallel to the longitudinal direction (i.e., the *c*-axis).

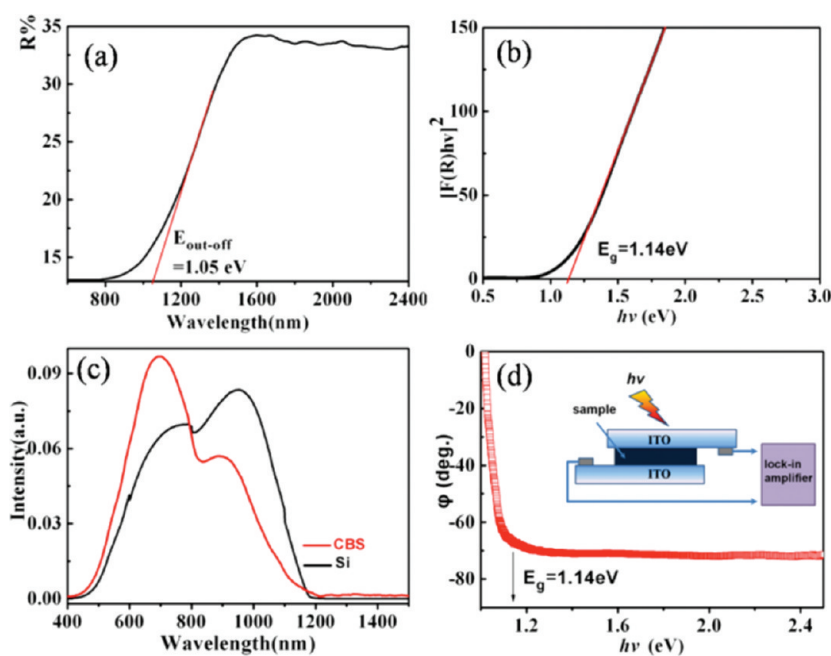


**Figure 8.** (a) UV–vis–NIR diffuse reflectance spectrum of the CBS nanoribbons film. (b) The  $F(R)^2$  versus  $h\nu$  plot, from which the band gap energy,  $E_g = 1.14$  eV, is determined. (c) Photovoltage spectra of the CBS nanoribbons and single-crystal Si.<sup>43</sup> (d) The phase spectrum of the CBS nanoribbons. (Inset shows the schematics of the setup for the SPV measurement.)

between DDA and the  $\text{Cu}_4\text{Bi}_4\text{S}_9$  framework. Note that, while the organoamine-assisted growth mechanism has been developed earlier for the synthesis of some binary inorganic or hybrid nanostructures,<sup>25,37</sup> the novelty of this work is to extend this method to the controllable synthesis of ultralong ternary chalcogenide nanoribbons.

Figure 8a shows the UV–vis–NIR diffuse reflectance spectrum of the as-obtained CBS nanoribbons. As seen, the nanoribbons have an absorption in the entire UV–vis range, with a very steep absorption edge at  $\sim 1100$  nm. For a direct bandgap semiconductor, the absorption coefficient can be described by the relationship<sup>38</sup>

$$F(R)^2 \propto h\nu$$

where  $F(R)$  is the Kubelka–Munk function ( $F(R) = (1 - R)^2 / (2R)$ ),  $R$  is the reflectance coefficient, and  $h\nu$  is the photo energy. A plot of  $F(R)^2$  against the photo energy for CBS nanoribbons is shown in Figure 8b. The exhibited parabolic band profile near the cutoff energy suggests that the CBS nanoribbons are direct transition semiconductors (also see Figure S5 in the Supporting Information). The band gap ( $E_g$ ) of CBS nanoribbons, estimated by extrapolating the curve in Figure 8b, is  $\sim 1.14$  eV. This value is close to the bandgap values used in most PV materials.

Surface photovoltage of semiconductors is generated from the spatial separation of photoinduced electron–hole pairs. What can be deduced from the study of SPV is not only the fundamental light absorption but also the behavior of photoinduced

charge carriers. SPV spectroscopy has been proved to be a powerful tool to study the optoelectronic properties of nanoscale semiconductor materials, as well as PV devices.<sup>39,40</sup> To test the potential PV applications of the CBS nanoribbons, SPV spectroscopy was conducted to the CBS nanoribbon film which was structured into a capacitor-type device.<sup>41,42</sup> For comparison, the SPV spectrum of a single-crystal silicon, the main-stream PV material in the current industry, was also measured under the same conditions. As shown in Figure 8c, the SPV response band of CBS nanoribbons spans from UV–vis to the near-infrared region (~1200 nm), which is comparable to that of the single-crystal silicon. Moreover, the CBS nanoribbons exhibit a higher SPV response intensity in the visible light region (500–780 nm) than in the near-infrared, which is just opposite to the case of silicon. These mean that the CBS nanoribbons have a full-visible solar spectrum SPV response, and higher photoinduced charge (electron–hole pairs) separation efficiency in the visible-light region than in the near-infrared. Hence, this material might provide a much broader choice and a potential alternative to many existing costly and/or toxic PV materials. The SPV onset of the CBS nanoribbons at ~1100 nm is consistent with the band edge observed in the UV–vis spectrum. Figure 8d shows the SPV phase spectrum of the CBS nanoribbons, from which the constant phase retardation of  $-70^\circ$  is clearly observed for  $h\nu > 1.14$  eV. This suggests that the SPV response of the CBS nanoribbons induced by the excitation of photons with  $h\nu > 1.14$  eV has the same attribute, viz, super bandgap SPV resulted from the band-to-band transition.<sup>27</sup>

## CONCLUSIONS

A large quantity of single-crystalline, semiconducting  $\text{Cu}_4\text{Bi}_4\text{S}_9$  nanoribbons have been fabricated using a facile solvothermal method. Control of the width-to-thickness ratio is realized by adjusting the concentration of a chemical linker, DDA. Optical investigations reveal that the as-prepared CBS nanoribbons are direct bandgap semiconductors, with evident light absorption and surface photovoltage response in the entire visible wavelength range. Also, as indicated by the SPV data, the photoinduced charge separation efficiency is higher in the visible range than that in the near-infrared. These data provide a proof-of-principle demonstration of the potential applications of these CBS nanoribbons in photovoltaic devices (e.g., solar absorber or photo-detectors).

## ASSOCIATED CONTENT

**S Supporting Information.** Additional SEM images, more discussion on the reaction process, and SPV results. (PDF) This material is available free of charge via the Internet at <http://pubs.acs.org/>.

## AUTHOR INFORMATION

### Corresponding Author

\*E-mails: [anlian.pan@gmail.com](mailto:anlian.pan@gmail.com) (A.P.), [ygwang@blem.ac.cn](mailto:ygwang@blem.ac.cn) (Y.W.), [fanhj@ntu.edu.sg](mailto:fanhj@ntu.edu.sg) (H.J.F.).

## ACKNOWLEDGMENT

This work was supported by the National Natural Science Foundation of China (Grant Nos. 90923014, 10974050, 60796078, 20903038, 10774174), and partly by “973” National

Key Basic Research Program of China (under Grant No. 2007CB310500), the Hunan Provincial Natural Science Fund (No. 09JJ1009), the Aid Program for Science and Technology Innovative Research Team in Higher Educational Institutions of Hunan Province.

## REFERENCES

- (1) Matthew, J. B.; Song, J. *Energy Environ. Sci.* **2009**, *2*, 1050–1059.
- (2) Huynh, W. U.; Dittmer, J. D.; Alivisatos, A. P. *Science* **2002**, *295*, 2425–2427.
- (3) Tsakalakos, L.; Balch, J.; Fronheiser, J.; Korevaar, B. A.; Sulima, O.; Rand, J. *Appl. Phys. Lett.* **2007**, *91*, 233117–233119.
- (4) Tian, B. Z.; Zheng, X. L.; Kempa, T. J.; Fang, Y.; Yu, N. F.; Yu, G. H.; Huang, J. L.; Lieber, C. M. *Nature* **2007**, *449*, 885–890.
- (5) Law, M.; Greene, L.; Johnson, J.; Saykally, R.; Yang, P. D. *Nat. Mater.* **2005**, *4*, 455–459.
- (6) Peng, H. L.; Schoen, D. T.; Meister, S.; Zhang, X. F.; Cui, Y. *J. Am. Chem. Soc.* **2007**, *129*, 34–35.
- (7) Wu, Y. Y.; Yang, P. D. *J. Am. Chem. Soc.* **2001**, *123*, 3165–3166.
- (8) Li, H. X.; Ma, H. Q.; Zeng, Y. P.; Pan, A. L.; Zhang, Q. L.; Yu, H. C.; Wang, T. H.; Wang, Y. G.; Zou, B. S. *J. Phys. Chem. C* **2010**, *114*, 1845–1848.
- (9) Wang, F. D.; Yu, H.; Jeong, S. S.; Pietryga, J. M.; Hollingsworth, J. A.; Gibbons, P. C.; Buhro, W. E. *ACS Nano* **2008**, *2*, 1903–1913.
- (10) Yang, J.; Xue, C.; Yu, S. H.; Zeng, J. H.; Qian, Y. T. *Angew. Chem., Int. Ed.* **2002**, *41*, 4697–4700.
- (11) Gou, X. L.; Cheng, F. Y.; Shi, Y. H.; Zhang, L.; Peng, S. J.; Chen, J.; Shen, P. W. *J. Am. Chem. Soc.* **2006**, *128*, 7222–7229.
- (12) Huang, J. Q.; Chiam, S. Y.; Tan, H. H.; Wang, S. J.; Chim, W. K. *Chem. Mater.* **2010**, *22*, 4111–116.
- (13) Meng, T. N.; Chris, B. B.; Jagade, J. V. *J. Am. Chem. Soc.* **2006**, *128*, 7118–7119.
- (14) Ward, J. S.; Ramanathan, K.; Hasoon, F. S.; Coutts, T. J.; Keane, J.; Contreras, M. A.; Moriarty, T.; Noufi, R. *Prog. Photovoltaics* **2002**, *10*, 41–46.
- (15) Riha, S. C.; Parkinson, B. A.; Prieto, A. L. *J. Am. Chem. Soc.* **2009**, *131*, 12054–12055.
- (16) Todorov, T. K.; Reuter, K. B.; Mitzi, D. B. *Adv. Mater.* **2010**, *22*, E156–E159.
- (17) Gerein, N. J.; Haber, J. A. *Chem. Mater.* **2006**, *18*, 6297–6302.
- (18) Estrella, V.; Nair, M.; Nair, P. K. *Semicond. Sci. Technol.* **2003**, *18*, 190–194.
- (19) Nair, P. K.; Huang, M. T.; Nair, L. S.; Hu, H. L.; Meyers, E. A.; Zingaro, R. A. *J. Mater. Res.* **1997**, *12*, 651–656.
- (20) Gerein, N. J.; Haber, J. A. *Chem. Mater.* **2006**, *18*, 6289–6296.
- (21) Kryukova, G.; Heuer, M.; Doering, T.; Bente, K. *J. Cryst. Growth* **2007**, *306*, 212–216.
- (22) Chen, D.; Shen, G. Z.; Tang, K. B.; Liu, X. M.; Qian, Y. T.; Zhou, G. *J. Cryst. Growth* **2003**, *253*, 512–516.
- (23) Zou, G. F.; Li, H.; Zhang, Y. G.; Xiong, K.; Qian, Y. T. *Nanotechnology* **2006**, *17*, S313–S320.
- (24) Gao, M. R.; Yao, W. T.; Yao, H. B.; Yu, S. H. *J. Am. Chem. Soc.* **2009**, *131*, 7486–7487.
- (25) Wang, D. S.; Hao, C. H.; Zheng, W.; Peng, Q.; Wang, T. H.; Liao, Z. M.; Yu, D. P.; Li, Y. D. *Adv. Mater.* **2008**, *20*, 2628–2632.
- (26) Zhang, X.; Zhang, L. Z.; Xie, T. F.; Wang, D. J. *J. Phys. Chem. C* **2009**, *113*, 7371–7378.
- (27) Kronik, L.; Shapira, Y. *Surf. Sci. Rep.* **1999**, *37*, 1–206.
- (28) Grigas, J.; Talik, E.; Lazauskas, V. *Phys. Status Solidi B* **2002**, *232*, 220–230.
- (29) Wu, C.; Hu, Z.; Wang, C.; Sheng, H.; Yang, J.; Xie, Y. *Appl. Phys. Lett.* **2007**, *91*, 143104–143106.
- (30) Liu, Z. P.; Peng, S.; Xie, Q.; Hu, Z. K.; Yang, Y.; Zhang, S. Y.; Qian, Y. T. *Adv. Mater.* **2003**, *15*, 936–940.
- (31) Wang, D. S.; Hao, C. H.; Zheng, W.; Ma, X. L.; Chu, D. R.; Peng, Q.; Li, Y. D. *Nano Res.* **2009**, *2*, 130–134.

(32) Bente, K.; Kupcik, V. *Acta Crystallogr., Sect. C: Cryst. Struct. Commun.* **1984**, *C40*, 1985–1986.

(33) Bente, K.; Kupcik, V.; Amthauer, G.; Siebert, D. *Acta Crystallogr., Sect. C: Cryst. Struct. Commun.* **1984**, *40*, C262–C262.

(34) Hartman, P.; Perdok, W. G. *Acta Crystallogr.* **1955**, *8*, 49–52.

(35) Liu, J. P.; Li, Y. Y.; Huang, X. T.; Li, Z. K.; Li, G. Y.; Zeng, H. B. *Chem. Mater.* **2008**, *20*, 250–257.

(36) Yao, H. B.; Gao, M. R.; Yu, S. H. *Nanoscale* **2010**, *2*, 323–334.

(37) Gao, Q. S.; Chen, P.; Zhang, Y. H.; Tang, Y. *Adv. Mater.* **2008**, *20*, 1837–1842.

(38) Chung, I.; Song, J.; Jang, J.; Freeman, A.; Ketterson, J.; Kanatzidis, M. J. *Am. Chem. Soc.* **2009**, *131*, 2647–2656.

(39) Zhao, Q. D.; Xie, T. F.; Peng, L. L.; Lin, Y. H.; Wang, P.; Peng, L.; Wang, D. J. *J. Phys. Chem. C* **2007**, *111* (45), 7136–7145.

(40) Gross, D.; Mora-Sero, I.; Dittrich, T.; Belaidi, A.; Mauser, C.; Houtepen, A. J.; Da-Como, E.; Rogach, A. L.; Feldmann, J. *J. Am. Chem. Soc.* **2010**, *132*, 5981–5983.

(41) Wu, Z. Y.; Wang, X. J.; Huang, Q. S. *Phys. Status Solidi B* **1999**, *213*, 343–348.

(42) Toušek, J.; Toušková, J.; Poruba, A. *Solar Energy Mater. Solar Cells* **2005**, *88*, 331–337.

(43) Note that the decrease of the SPV response below the wavelength of 600 nm is due to the decrease of the luminous energy of the halogen-tungsten lamp in this spectrum region (See Figure S4 in the Supporting Information). The dips at ~820 nm in the SPV response spectra are due to a switch of the filters at this wavelength during the measurement.